The role of initial magnetic field structure in the launching of protostellar jets

Isabella A. Gerrard [1,2]★ Christoph Federrath[1] and Rajika Kuruwita[1]

[1]*Research School of Astronomy and Astrophysics, Australian National University, Canberra, ACT 2611, Australia*
[2]*Monash Centre for Astrophysics, Monash University, Clayton, VIC 3800, Australia*

ABSTRACT

Magnetic fields are known to play a crucial role in the star formation process, particularly in the formation of jets and outflows from protostellar discs. The magnetic field structure in star-forming regions is not always uniform and ordered, often containing regions of magnetic turbulence. We present grid-based, magnetohydrodynamical simulations of the collapse of a $1\,M_{\odot}$ cloud core, to investigate the influence of complex magnetic field structures on outflow formation, morphology, and efficiency. We compare three cases: a uniform field, a partially turbulent field and a fully turbulent field, with the same magnetic energy in all three cases. We find that collimated jets are produced in the uniform-field case, driven by a magneto-centrifugal mechanism. Outflows also form in the partially turbulent case, although weaker and less collimated, with an asymmetric morphology. The outflows launched from the partially turbulent case carry the same amount of mass as the uniform-field case but at lower speeds, having only have 71 per cent of the momentum of the uniform-field case. In the case of a fully turbulent field, we find no significant outflows at all. Moreover, the turbulent magnetic field initially reduces the accretion rate and later induces fragmentation of the disc, forming multiple protostars. We conclude that a uniform poloidal component of the magnetic field is necessary for the driving of jets.

Key words: magnetic fields – MHD – turbulence – stars: formation – stars: jets.

1 INTRODUCTION

Stars form in giant molecular clouds (GMCs) (Elmegreen & Scalo 2004; Mac Low & Klessen 2004; McKee & Ostriker 2007; Hennebelle & Falgarone 2012), which are ubiquitously permeated by magnetic fields (Crutcher 2012) and are observed to be inherently turbulent (Larson 1981; Dubinski, Narayan & Phillips 1995; Ossenkopf & Mac Low 2002; Heyer & Brunt 2004; Roman-Duval et al. 2011; Hennebelle & Falgarone 2012). In the last decade, it has become clear that turbulence and magnetic fields are vital prerequisites for star formation (Mac Low & Klessen 2004; McKee & Ostriker 2007; Federrath & Klessen 2012; Joos et al. 2013; Li et al. 2014a; Padoan et al. 2014; Federrath 2015). Observations of large- and small-scale magnetic field structures in GMCs are inferred by mapping dust polarization. Dust grains align themselves perpendicular to the local magnetic field lines (Lazarian & Hoang 2007), and the resultant polarized thermal emission can then be observed as a tracer of the field structure (Planck Collaboration XXXIII 2016). Observations of dust polarization in GMCs have recently revealed turbulent magnetic field structures in star-forming cores (Girart et al. 2013; Ching et al. 2017; Hull et al. 2017; King

et al. 2018), as well as cores threaded with distinctly uniform fields (Chapman et al. 2013; Pattle et al. 2017). Although the intricacies of the dust alignment mechanism make extracting the *exact* magnetic field morphology from polarization maps difficult (King et al. 2018), the technique has demonstrated that magnetic fields in star-forming cores and throughout the Universe are complex structures that vary from uniform and ordered to tangled and chaotic (Cox et al. 2018).

The formation of jets and outflows during star formation has been proposed as a partial solution to some of the ongoing problems of star formation theory (Pudritz & Norman 1986; Crutcher 1999). Bipolar jets and outflows carry angular momentum away from the protostellar disc, which accounts for the relatively slow rotation rates of stars (Pudritz et al. 2007; Joos, Hennebelle & Ciardi 2012; Frank et al. 2014). These jets also transport mass away from the accretion disc, which impacts the star formation efficiency (SFE) and may help to explain low star formation rates (Price & Bate 2009; Krumholz 2014; Padoan et al. 2014; Federrath 2015). Driven by magnetic pressure (Lynden-Bell 2003), and in some cases accelerated by the magneto-centrifugal mechanism (Blandford & Payne 1982), these bipolar outflows and jets can extend up to several parsecs (Stojimirović et al. 2006). Herbig–Haro objects with distinctive bipolar outflows are observational confirmation of this phase of star formation (Bally & Reipurth 2001; Wu et al. 2004). The distinction between jets and outflows in the literature is somewhat

★ E-mail: isabella.gerrard@monash.edu

ambiguous; while it is true that all jets are outflows of a particular kind, not all outflows are fast, collimated and jet-like. We will refer to high-speed outflows exhibiting high degrees of collimation as jets and those with less distinct structure as outflows, although this is a purely qualitative distinction.

The majority of the computational work simulating the launching of jets and outflows during star formation has used ordered magnetic fields of varying strength (Banerjee & Pudritz 2006; Machida et al. 2006; Shang et al. 2006; Price & Bate 2007; Hennebelle & Fromang 2008; Machida, Inutsuka & Matsumoto 2008; Price, Tricco & Bate 2012; Bate, Tricco & Price 2014). We use the term ordered to refer to fields that are uniform and aligned with the rotation axis of the accretion disc. There has been some work done on the effects of a misaligned magnetic field (one which is still uniform but the angle between the disc rotation axis and the mean component of the field is non-zero) (Hennebelle & Ciardi 2009; Joos et al. 2012; Krumholz, Crutcher & Hull 2013; Li, Krasnopolsky & Shang 2013; Lewis, Bate & Price 2015; Lewis & Bate 2017). Lewis et al. (2015) used smoothed particle magnetohydrodynamics to model the collapse of a magnetized cloud core and found that collimated jets are produced with shallow alignment angles ($<10°$), and that no discernible outflows were produced with angles greater than $60°$. Their work is in agreement with that of Ciardi & Hennebelle (2010), who carried out adaptive mesh refinement (AMR), magnetohydrodynamical (MHD) simulations with similar results, showing that all outflowing material was suppressed if the field was aligned perpendicular to the rotation axis. The orientation of the field relative to the rotation axis also effects the formation and survival of protostellar discs (Li et al. 2014b; Gray, McKee & Klein 2018). However, the role of turbulent magnetic field structures has not been quantified in previous work.

Here, we carry out a controlled numerical experiment to ascertain what effect an initially turbulent magnetic field has on the early stages of jet and outflow formation. This experiment has been designed such that the only parameter that varies is the *structure* of the magnetic field. Our numerical methods are described in Section 2, the results and analysis of which are presented in Section 3. The implications of these results are discussed in Section 4. In Section 5, we present our conclusions and summarize the outlook for future work.

2 METHODS

We carry out MHD simulations of protostellar disc and star formation. We compare a set of three different simulations, which only differ in their initial magnetic field structure. The first is a control simulation in which the magnetic field is initially ordered and aligned with the *z*-component of angular momentum, hereafter uniform. The second is constructed so as to affect equally ordered and unordered components of the magnetic field (see Section 2.3.2) with the mean field component aligned as in the ordered case, hereafter partially turbulent. The third simulation starts with a fully turbulent field without any ordered, mean component, hereafter fully turbulent.

We compare these three simulations to study the effects of the turbulent field structure. All other aspects of the set-up are identical in the three simulations, closely following those of Federrath et al. (2014) and Kuruwita, Federrath & Ireland (2017), which are summarized below.

2.1 FLASH

We use FLASH, a grid-based, adaptive mesh refinement (AMR) code (Fryxell et al. 2000; Dubey et al. 2008). The refinement criteria

is based on the Jeans length, such that the mesh is refined in regions where the Jeans length is resolved within less than 32 grid cells (Sur et al. 2010; Federrath et al. 2011b, 2014). This ensures that the Jeans length is always resolved everywhere in at least 32 grid cells. We use the positive-definite HLL3R Riemann scheme (Waagan, Federrath & Klingenberg 2011) to solve the standard set of 3D, ideal MHD equations:

$$\frac{\partial \rho}{\partial t} + \nabla \cdot (\rho \, \boldsymbol{v}) = 0, \tag{1}$$

$$\rho \left(\frac{\partial}{\partial t} + \boldsymbol{v} \cdot \nabla \right) \boldsymbol{v} = \frac{(\boldsymbol{B} \cdot \nabla) \, \boldsymbol{B}}{4\pi} - \nabla P_{\text{tot}} + \rho \, \boldsymbol{g}, \tag{2}$$

$$\frac{\partial E}{\partial t} + \nabla \cdot \left((E + P_{\text{tot}}) \, \boldsymbol{v} - \frac{(\boldsymbol{B} \cdot \boldsymbol{v}) \, \boldsymbol{B}}{4\pi} \right) = \rho \, \boldsymbol{v} \cdot \boldsymbol{g}, \tag{3}$$

$$\frac{\partial \boldsymbol{B}}{\partial t} = \nabla \times (\boldsymbol{v} \times \boldsymbol{B}), \tag{4}$$

$$\nabla \cdot \boldsymbol{B} = 0, \tag{5}$$

where ρ, $\boldsymbol{v}$, $\boldsymbol{B}$, $\boldsymbol{g}$, and E denote the gas density, velocity, magnetic field strength, gravitational acceleration of the gas, and total energy density (internal, plus magnetic, plus kinetic), respectively.

The div(B) constraint is enforced by a parabolic divergence cleaning method following the basic concept of Marder (1987). However, we have also tested divergence cleaning schemes that combine parabolic and hyperbolic cleaning, by Dedner et al. (2002) and with recent modifications by Tricco, Price & Bate (2016). For our particular problem set-up, these schemes provide similar results and performance. The div(B) cleaning scheme used here was tested in Waagan et al. (2011) and yields reasonable results; i.e. while none of these cleaning schemes yield div(B) to machine precision everywhere and at all times (as opposed to Constrained Transport; see Evans & Hawley 1988 and Gardiner & Stone 2005), the errors introduced due to div(B) waves are negligible and do not affect our results and conclusions.

P_{tot} denotes the sum of the magnetic and thermal pressure, where the magnetic pressure is given by

$$P_{\text{B}} = \frac{|\boldsymbol{B}|^2}{8\pi}. \tag{6}$$

To define the thermal pressure P_{th}, we adopt a piecewise polytropic equation of state with Γ values derived from the detailed radiation-hydrodynamic simulations of Masunaga & Inutsuka (2000):

$$P_{\text{th}} = K \rho^{\Gamma}, \tag{7}$$

where Γ is defined by

$$\Gamma = \begin{cases} 1.0 \text{ for } & \rho \leq \rho_1 \equiv 2.50 \times 10^{-16} \, \text{g cm}^{-3}, \\ 1.1 \text{ for } \rho_1 < \rho \leq \rho_2 \equiv 3.84 \times 10^{-13} \, \text{g cm}^{-3}, \\ 1.4 \text{ for } \rho_2 < \rho \leq \rho_3 \equiv 3.84 \times 10^{-8} \, \text{g cm}^{-3}, \\ 1.1 \text{ for } \rho_3 < \rho \leq \rho_4 \equiv 3.84 \times 10^{-3} \, \text{g cm}^{-3}, \\ 5/3 \text{ for } & \rho > \rho_4. \end{cases} \tag{8}$$

These polytropic exponents affect radiative transfer on the local cell scale, tracking the initial isothermal contraction, adiabatic heating of the first core, H_2 dissociation in the second collapse leading to the second core, and then return to adiabatic heating. The polytropic constant K is then adjusted according to the density in each regime of equation (8) such that $K = c_s^2$, so that the sound speed c_s and

temperature are continuous functions of density. In the isothermal regime when $\Gamma = 1$, we define the sound speed in the gas to be 2.0×10^4 cm s^{-1}, which corresponds to a temperature of 11 K and a mean molecular weight of $2.3m_H$. The polytropic constant is $K \equiv 4.0 \times 10^8$ cm^2 s^{-2}. For a dense molecular gas of solar metallicity, $\rho \leq 2.50 \times 10^{-16}$ g cm^{-3} is a good approximation for the initial isothermal evolution for a wide range of densities (Wolfire et al. 1995; Omukai et al. 2005; Pavlovski, Smith & Mac Low 2006; Glover & Mac Low 2007b,a; Glover et al. 2010; Hill et al. 2011; Glover & Clark 2012; Hennemann et al. 2012). The gravitational acceleration of the gas, $\boldsymbol{g}$, is comprised of the gravitational potential of the gas and the contribution of any sink particles (described in Section 2.2) which may be formed. It is therefore defined as

$$\boldsymbol{g} = -\nabla\Phi_{\text{gas}} + \boldsymbol{g}_{\text{sinks}}. \tag{9}$$

We use a tree-based OctTree algorithm to calculate the gravitational interaction of the gas (Wünsch et al. 2018), and direct N-body summations to calculate the gas–sink interactions (Federrath et al. 2014).

2.2 Sink particles

Truelove et al. (1997) found that the Jeans length must be resolved within four grid cells to avoid artificial fragmentation. Using sink particles ensures that resultant protostars are not numerical artefacts, allows us to advance our simulations beyond the point of first collapse, and also enables us to quantify the star formation rate and SFE (Federrath et al. 2010b). We therefore define the density threshold for sink particle creation as

$$\rho_{\text{sink}} = \frac{\pi c_s^2}{4Gr_{\text{sink}}^2} \, , \tag{10}$$

where $r_{\text{sink}} = 2.5\Delta x$, Δx being defined as the cell length on the maximum AMR level. In our simulation ,$\Delta x = 3.05$ au (see Section 4.3.3). The critical density for sink formation at the highest level of refinement is $\rho_{\text{sink}} = 9.15 \times 10^{-11}$ g cm^{-3}, which is iteratively calculated via equations (10) and (8), as the sound speed is a function of density. Once a cell has reached this density threshold, a control volume of radius r_{sink} is created around that cell. If the gas inside the control volume meets the following criteria, described by Federrath et al. (2010b), a sink particle is created:

(i) The cell with $\rho \geq \rho_{\text{sink}}$ is on the highest level of AMR,
(ii) No other sink particle is within r_{sink} of the control volume,
(iii) The gas is converging from all directions, ($v_r < 0$),
(iv) The gas is bound such that $|E_{\text{grav}}| > E_{\text{th}} + E_{\text{kin}} + E_{\text{mag}}$,
(v) The volume has a gravitational minimum at its centre,
(vi) The gas is Jeans unstable.

Once a sink particle is created, it is then able to accrete gas, provided that gas has exceeded the density threshold within the accretion radius of the sink and the gas is bound and collapsing towards the sink particle. The accreted gas is removed from the MHD system and added to the sink particle, such that the total mass, the centre of mass, and the linear and angular momenta are conserved. This process is described in detail by Federrath et al. (2014).

2.3 Initial conditions

Following initial conditions similar to those of Federrath et al. (2014) and Kuruwita et al. (2017), our computational domain is a box of size 1.2×10^{17} cm, or 8000 au on each side. It contains

Table 1. Construction of the magnetic field in each simulation. All other parameters are identical in each model (see Section 2.3 for details). Columns: (1) simulation name, (2) fraction of the field which is uniform, (3) fraction of the field which is un-ordered (turbulent), and (4) total rms field strength.

Simulation name	Uniform component (%)	Turbulent component (%)	Total RMS field strength (μG)
Uniform	100	–	100
Partially turbulent	50	50	100
Fully turbulent	–	100	100

a $1\,M_\odot$ gas cloud of radius 3300 au with uniform density of $\rho_0 = 3.82 \times 10^{-18}$ g cm^{-3}. So that the cloud is well defined, the gas density outside the cloud is $\rho_0/100$, with internal energy such that the cloud is in pressure equilibrium with its surroundings. The cloud is given solid body rotation with angular momentum of 1.85×10^{51} g cm^2 s^{-1}, which corresponds to a ratio of rotational energy to gravitational energy of $\beta_{\text{rot}} \approx 0.01$ (Lewis & Bate 2018). It is important to note that the initial conditions are identical across the three models, with the sole exception of the magnetic field structure. The construction of the magnetic field in each of the three models is summarized in Table 1, and visualized in the top panel of Fig. 1.

2.3.1 Constructing the uniform magnetic field

In the uniform case, the total magnetic field threaded through this cloud is 100 μG in magnitude. This field is oriented parallel to the rotation axis of the cloud and evenly distributed. The mass-to-flux ratio is given by $(M/\Phi)/(M/\Phi)_{\text{crit}} = 5.2$, where the critical mass-to-flux ratio is 487 g cm^{-2} G^{-1} as defined by Mouschovias & Spitzer (1976).

2.3.2 Constructing the partially turbulent magnetic field

In the partially turbulent case, the magnetic field has both an initially uniform and turbulent components. The turbulent component is constructed using the same method as is described in Section 2.3.3. The overall magnitude of the field remains constant and consistent with the other two cases. The total field is given by

$$B = B_0 + \delta B, \tag{11}$$

where B_0 is the uniform component and δB is the perturbation or turbulent field component. We set the magnetic energy (proportional B^2) of the uniform and turbulent components to be equal. Consistency with our other two cases requires the total field to be $100\,\mu$G, so

$$\langle B^2 \rangle = (100\,\mu\text{G})^2, \tag{12}$$

which gives

$$B_0 = \frac{\sqrt{2}}{2} \times 100\,\mu\text{G} \tag{13}$$

$$\left[\langle(\delta B)^2\rangle\right]^{\frac{1}{2}} = \frac{\sqrt{2}}{2} \times 100\mu\text{G} \tag{14}$$

giving each component a value of 70.7 μG.

2.3.3 Constructing the fully turbulent magnetic field

As outlined in Section 2.3, the partially turbulent and fully turbulent cases have turbulent magnetic field structures. We do not drive
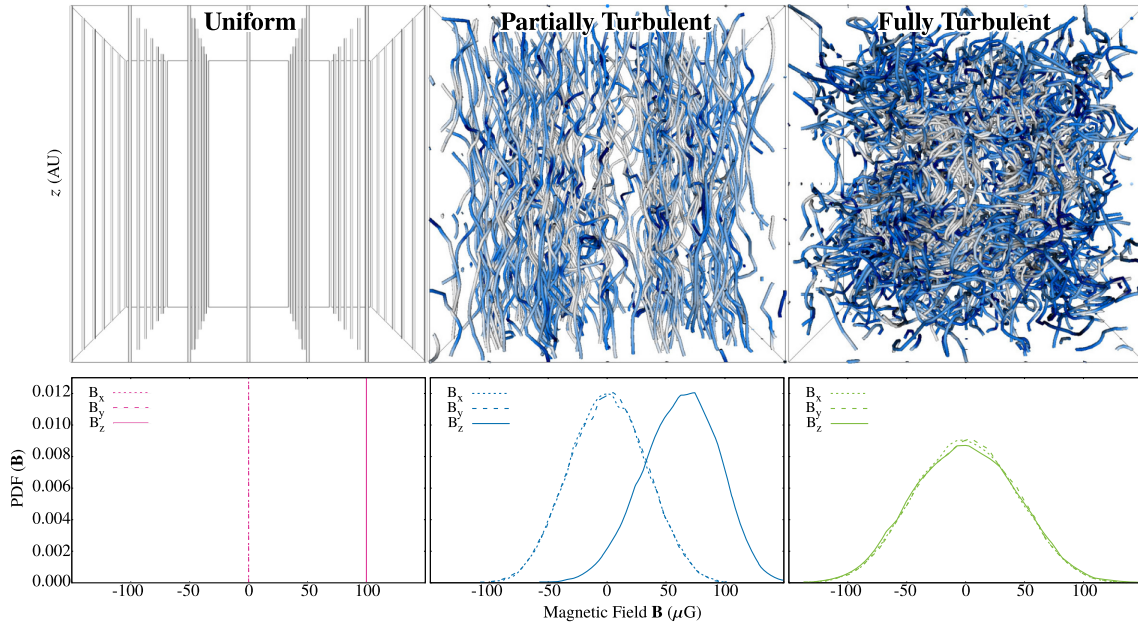
Figure 1. Top: 3D visual representation of the initial magnetic field structure in our three simulation cases: uniform (left), partially turbulent (middle), and fully turbulent (right). Each panel shows the entire simulation domain (8000 au on each side), and a sample of the field structure. The colouring of the field lines is an arbitrary consequence of the 3D rendering used and does not reflect field strength. Bottom: Probability density functions (PDFs) of the initial magnetic field components (in B_x, B_y, B_z) for each of the three simulation models, respectively. The vertical lines in the uniform model are delta functions, i.e. $B_x = B_y = 0$ and $B_z = 100\,\mu$G. For the partially turbulent and fully turbulent models, the field distributions are Gaussian as imposed by the turbulent field construction method (see Section 2.3.3 for details). Note that the total RMS magnetic field strength is identical with 100 μG in all three simulation cases, such that our study probes the consequences of different magnetic field structure (with the overall strength of the field held constant).

turbulence in the field, but rather construct the initial conditions such that the field vectors are randomly orientated. Here, we employ a Kazantsev power-law spectrum with an exponent of 3/2 as the Fourier decomposition of the turbulent field (Brandenburg & Subramanian 2005; Federrath 2016). The basic Fourier technique for constructing turbulent vector fields follows the method described in Federrath et al. (2010a). The range of the wavenumber k, in units of $2\pi/L$, is within $2 < k < 10$, where L is the length of the box. This constrains the spectrum to the range $4\pi/L$ to $20\pi/L$. The Kazantsev spectrum is the result of turbulent dynamo amplification (Kazantsev 1968; Federrath et al. 2011a). This is particularly important because field amplification via the turbulent dynamo acts initially on the small-scale seeds of a magnetic field (Brandenburg & Subramanian 2005; Schober et al. 2012b,a; Schleicher et al. 2013).

3 RESULTS

As the proper time elapsed in each simulation varied between our models, we have chosen to compare the three simulations matched on star formation efficiency rather than time. We define SFE as

$$\mathrm{SFE} = \frac{M_{\mathrm{sinks}}}{M_{\mathrm{tot}}}, \qquad (15)$$

where M_{sinks} is the total mass contained in sink particles and M_{tot} is the initial gas mass of the cloud (1 $M_\odot$). This is discussed further in Section 4.

3.1 Time evolution of protostellar mass

As the simulations evolve, the spherical gas cloud collapses into an accretion disc in the centre of the domain. The disc structure is a fundamental result of the conservation of angular momentum.
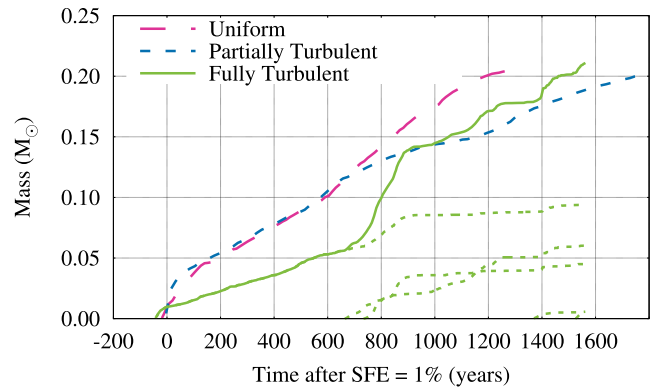

Figure 2. Evolution of the sink particle masses in each of the three models. The magenta long-dashed line is the uniform case and the blue short-dashed line is the partially turbulent case. The solid green line is the fully turbulent model and shows the sum of accreted mass in each sink particle, while the dotted lines indicate the mass evolution of each individual sink particle in this model. Each model is scaled such that time = 0 corresponds to the time when SFE = 1 per cent in each model. As shown in the figure, each simulation was run until the mass in sink particles reached 0.2 $M_\odot$ or SFE = 20 per cent.

Within this protostellar disc, sink particles form. The uniform case formed exactly one sink particle at the centre of the domain. The partially turbulent case also produces a singular sink particle, approximately 8 au off centre. The fully turbulent case produces a total of five sinks, each forming at different times (Fig. 2). The mass evolution of the sink particles in each model is shown in Fig. 2.

The first and most massive sink particle in the fully turbulent case forms 9 au from the centre, with each subsequent particle

forming within 52 au of the first. Perturbations in the gas caused by the turbulent magnetic field result in real fragmentation of the disc, evident in the multiplicity of the fully turbulent model and the off-centre sink formation in the partially turbulent case.

The turbulent magnetic field produces a more isotropic magnetic pressure across the domain. This has implications for the magnitude of the magnetic pressure gradient at the epicentre of collapse as the gas is less efficient at condensing the field lines in the disc, delaying star formation in the fully turbulent case. Consequently, there is initially low SFE, which is illustrated by the shallow gradient of the fully turbulent model in Fig. 2. SFE reaches 20 per cent after 1200, 1800, and 1500 yr in the uniform, partially turbulent, and fully turbulent cases, respectively.

In summary, we find that the turbulent field component has a substantial impact on the evolution of the protostellar mass and on the fragmentation of the disc.

3.2 Jet and outflow morphology

In Fig. 3, we visualise the evolution of density slices, with magnetic field lines and velocity vectors superimposed. The colour scale in Fig. 3 shows the average density in the xz-plane of a slice of the domain. The slices are centred on (0,0,0), and have dimension of ± 1100 au in the x-, ± 100 au in the y- and ± 1100 au in the z direction.

Fig. 3 illustrates that the uniform case and the partially turbulent case produce definite jets and outflows, respectively. As expected, the uniform case produces collimated jets consistent with previous works, whereas collimation does not dominate the outflows of the partially turbulent case, which are asymmetric and 'lobe-like'. Most importantly, we find that jets are completely absent in the fully turbulent case. The mechanisms that drive the variance in jet and outflow morphology are discussed in Section 4.1.

3.3 Jet and outflow efficiency

Fig. 4 corroborates the visual evidence in Fig. 3. Here, we see the behaviour of material in two cylindrical analysis volumes defined as follows. The two cylindrical volumes begin 100 au above and below the centre of mass of the system, with a radius of 500 au and height of 1000 au. As Fig. 3 shows, these two cylinders well encompass the outflow region, enabling us to quantify the mass and momentum of the outflowing material. Outflowing material is defined as any cell in which $v_z > 0$ for $z > 0$ and $v_z < 0$ for $z < 0$.

As indicated in the top panel of Fig. 4, jets begin around 100 yr after SFE reaches 1 per cent in the uniform case, while in the partially turbulent case the outflow begins 100 yr before. Although the partially turbulent outflows start first, the amount of outflowing mass in the uniform case quickly matches that in the partially turbulent case. The momentum of the uniform jets similarly exceeds the partially turbulent outflows after 300 yr. This confirms the visual evidence in Fig. 3 that the partially turbulent case is less efficient at expelling mass from the disc than the uniform case. 500 yr after SFE = 1 per cent the outflowing material has characteristic velocities of $3.16 \, \mathrm{km \, s^{-1}}$ in the uniform case, $1.78 \, \mathrm{km \, s^{-1}}$ in the partially turbulent case and $0.32 \, \mathrm{km \, s^{-1}}$ in the fully turbulent case. These outflow speeds are lower than the $> 10 \, \mathrm{km \, s^{-1}}$ often found in observations, however, the outflows here are measured relatively close to the disc and at early times; they are still gaining speed and momentum. The outflow speeds in the uniform and partially turbulent cases are consistent with the speeds measured in other numerical studies of first core outflows (Tomida et al. 2010; Bate

et al. 2014; Vaytet et al. 2018; Wurster, Bate & Price 2018a). For example, in comparable simulations Bate et al. (2014) find outflow speeds from the first core to be $1.2 - 1.8$ and $1.0 - 2.5 \, \mathrm{km \, s^{-1}}$ for initial field strengths of 81 and $163 \, \mu\mathrm{G}$, respectively.

To compare the outflow efficiency of the partially turbulent and fully turbulent models to that of the uniform model, we take the ratio of the time-averaged value of the outflow quantities for each pair. That is,

$$\langle q(t) \rangle = \frac{\int_{t=-200\,\mathrm{yr}}^{t=1200\,\mathrm{yr}} q(t)\mathrm{d}t}{\int_{t=-200\,\mathrm{yr}}^{t=1200\,\mathrm{yr}} \mathrm{d}t}, \qquad (16)$$

where $q(t)$ is outflow mass or momentum. As the uniform case is intended to be the control run, we quantify the efficiency of each model by comparing $\langle q(t) \rangle$ for mass and momentum in the partially turbulent and fully turbulent cases to the uniform case. We find that the relative fraction of outflowing mass in the partially turbulent and fully turbulent cases are 100 per cent and 0.022 per cent, respectively. Compared to the uniform model, the momentum of outflows is 71 per cent and 0.0045 per cent for the partially turbulent and fully turbulent cases. This is summarized in Table 2. While the amount of outflowing mass in uniform and partially turbulent cases is comparable, the partially turbulent case takes approximately 200 yr longer to achieve this, making the jet in the uniform case the most efficient at transporting mass away from the disc. This is due to the high speeds of the jet material in the uniform case. In contrast, we find no significant outflow in the fully turbulent case, making it the least efficient at ejecting material.

4 DISCUSSION

Our study is designed to isolate and examine the contribution of initial magnetic field structure, to the complex balance of forces that govern star formation. As shown in Section 3, only the models with some ordered, poloidal component of the field produce jets and outflows.

4.1 Jet launching mechanisms

To explain the variance in outflow efficiency and morphology between our three models, we must examine the physical mechanisms by which protostellar jets and outflows are launched. It is possible to launch outflows via the force provided by a magnetic pressure gradient (Lynden-Bell 2003), although the morphology of an outflow driven solely by this mechanism need not be collimated or orientated perpendicular to the accretion disc. Collimated jets are driven by the magneto-centrifugal mechanism (Blandford & Payne 1982). In this model, the rotation of the accretion disc 'coils up' the magnetic field, concentrating the field lines in the disc which provides a magnetic pressure gradient, as well as a centrifugal force from the rotation. This mechanism is described by Blandford & Payne (1982) to form jets only if the poloidal component of the field makes an angle of $\geq 30°$ with the rotation axis, and the poloidal component of the field above and below the disc dominates any toroidal contribution to the field within the disc. The combination of these forces accelerates the gas along the field lines and forms collimated bipolar jets along the rotation axis of the disc.

Given the efficiency and high degree of collimation of jets in the uniform model, evident in Fig. 3, and given that the work of Blandford & Payne (1982) assumed a uniform field oriented along the rotation axis of the disc, we conclude that this is the driving
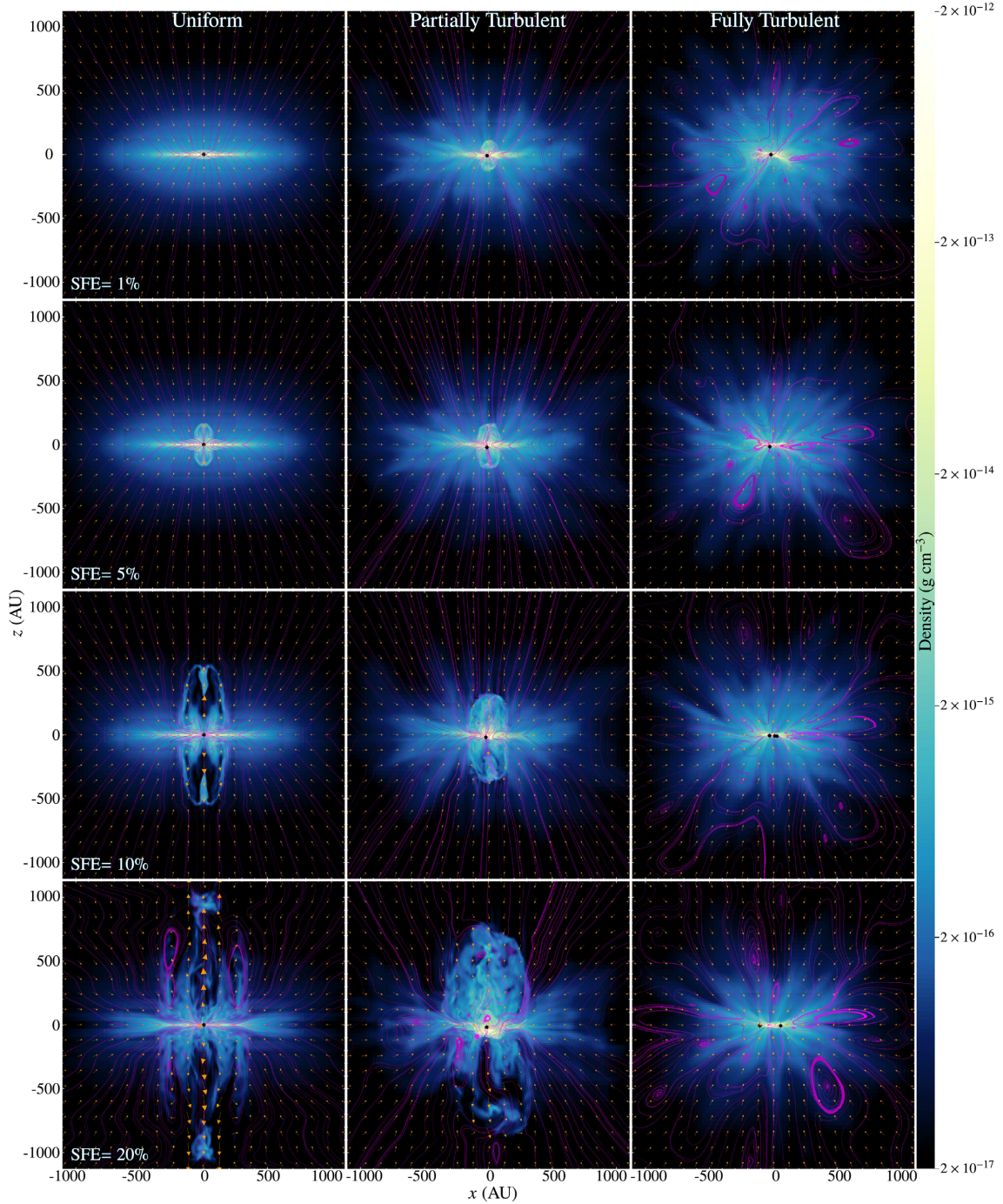
Figure 3. Visualizations in the *xz*-plane of the evolution of each model. They are matched on SFE, such that 'time' increases from top to bottom. The colour scale shows the average gas density within a 3D slice of dimensions (2200,100,2200) au. Each slice is centred on (0,0,0) au. The left column shows the evolution of the uniform model, the middle column shows the partially turbulent model and the right column shows the fully turbulent model. The magenta streamlines trace the magnetic field structure. The orange vectors represent the velocity field. The scaling of the vectors goes as the square root of the magnitude of the velocity, such that an arrow of length 100 au corresponds to a velocity of $10\,\mathrm{km\,s^{-1}}$. Sink particles are shown as black crossed spheres.

mechanism of the jets in our uniform model. This is corroborated by the tightly coiled structure of the field lines, seen in Fig. 5, which shows the same features as Fig. 3 at SFE = 10 per cent but in the *xy*-plane. Our partially turbulent model produced asymmetric, wide-angle outflows which were less efficient at transporting mass and momentum away from the disc than the jets in the uniform model. We conclude that the launching mechanism of the outflows

in the partially turbulent case is dominated by magnetic pressure gradients, although a weak magneto-centrifugal mechanism is likely still contributing since there is some poloidal component to the field, and the outflows are weakly collimated. In this case, the field lines are less uniformly and tightly coiled (Fig. 5), which suggests that the magneto-centrifugal mechanism plays a lesser role in launching the outflow than in the uniform case.
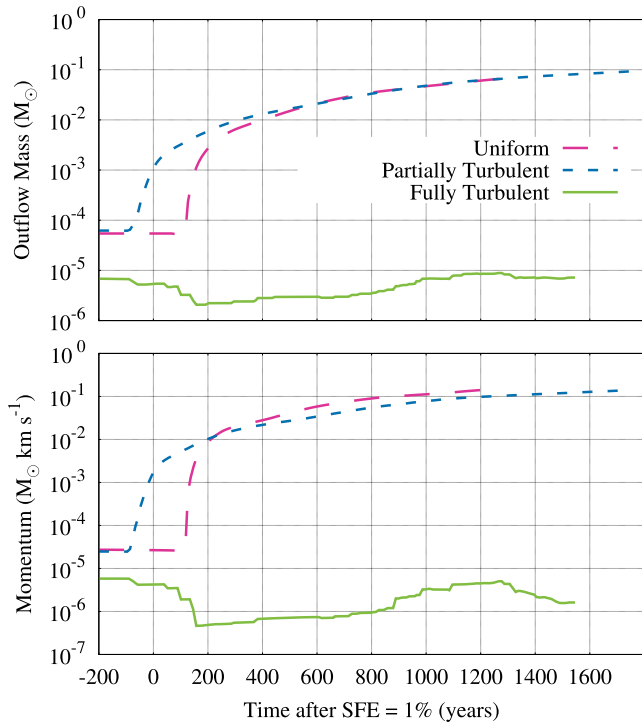
Figure 4. The time evolution of outflowing mass (top) and outflow momentum (bottom) for each model, beginning when SFE = 1 per cent. Jets in the uniform case (magenta long-dashed line) launch around 100 years after SFE = 1 per cent. Consistent with Fig. 3, outflows in the partially turbulent case (blue short-dashed line) begin to form 100 yr before SFE = 1 per cent. The partially turbulent case is less efficient in momentum but similar in outflowing mass to the uniform case, and there is no distinct outflowing material in the fully turbulent case (green solid line).

As seen in Figs 3 and 4, there was no distinctly outflowing material in the fully turbulent model. At SFE = 20 per cent, it is evident in the velocity field that material is still predominantly infalling. We conclude that the chaotic field structure has inhibited the launching of any outflow in the fully turbulent case. The absence of a uniform poloidal field component, not the presence of the turbulent field, inhibits the Blandford & Payne (1982) mechanism and does not allow for the formation of fast collimated jets. This is corroborated by the lack of a coiled field structure in Fig. 5. However, we also did not find any significant less collimated outflow in this case; this indicates that the magnetic pressure gradient is not (yet) strong enough to revert the collapse. This implies that a poloidal field component is essential for jet and outflow formation.

Fig. 6 shows the relative fraction of poloidal and toroidal field components to the total field strength in each of the three simulations. It becomes evident that the fully turbulent case contains no clearly ordered poloidal or toroidal structure in its field. Conversely, Fig. 6 reveals the poloidal field at the centre of the jet in the uniform

model and also in the outflow in the partially turbulent model. The prominent toroidal, 'cage-like' structure expected as a result of the winding of field lines in the magneto-centrifugal mechanism is also seen in these two cases. Figs 5 and 6 combined make a convincing argument for the jets and outflows in the uniform and partially turbulent models being driven by a combination of magnetic pressure gradients and the magneto-centrifugal mechanism.

4.2 Star formation and multiplicity

In the fully turbulent case, the turbulent magnetic field causes perturbations in the gas density due to locally varying magnetic pressure gradients. This perturbs the cloud, but an additional consequence is the isotropy of magnetic pressure, as compared to the uniform and partially turbulent cases, because the field has no mean component. In the context of the work of Price & Bate (2007), fragmentation is an expected consequence of this density perturbation, but the time delay of multiple protostar formation and accretion is also expected, due to the extra support of the isotropic magnetic pressure. This core ultimately fragments into five sink particles (as seen in Fig. 2). The sink particle formulation discussed in Section 2.2 ensures that this fragmentation is not a numerical artefact. Combined with the large body of evidence that multiplicity is ubiquitous in star formation (Duchêne & Kraus 2013; Bate 2015), it is unsurprising that the fully turbulent model produced multiple protostars.

Although we have chosen to match our simulations on SFE rather than absolute time, we can report that there is a significant time delay of 230 yr between the formation of the sink particles in the uniform and partially turbulent cases, with the protostar forming later in the partially turbulent case. In the reference time frame of Fig. 4, the relative time difference between jet and outflow launching in these two simulations is also of the order of 200 yr. This means that the outflows in each case form at approximately the same absolute time, and that the sink particle in the partially turbulent case forms after its outflow is launched. However, SFE quickly reaches 1 per cent, explained by the strong initial phase of accretion as evident in Fig. 2. The delay in sink particle formation and the high accretion rate in the partially turbulent case are a result of the turbulent component of the magnetic field. As in the fully turbulent case, the isotropy of magnetic pressure supports the core against collapse, which allows material to be concentrated in the disc while suppressing star formation. Eventually, the gravitational force overcomes the magnetic pressure, and a sink particle forms. There is then a large reservoir of material available for accretion, resulting in a steep increase in SFE.

4.3 Caveats

4.3.1 Non-ideal MHD

Our calculations do not include non-ideal MHD effects, which can lead to the suppression or distortions of outflows (e.g. Wurster, Price & Bate 2016; Wurster, Bate & Price 2018b). The smallest

Table 2. Normalized efficiency of outflow quantities. The quantities in the uniform model are normalised to 100 per cent efficiency so that the relative efficiency of the partially turbulent and fully turbulent models can be calculated. Columns: (1) model name, (2) relative fraction of outflow mass, (3) relative fraction of outflow momentum, (4) sink formation time (absolute time), and (5) launching time (absolute time).

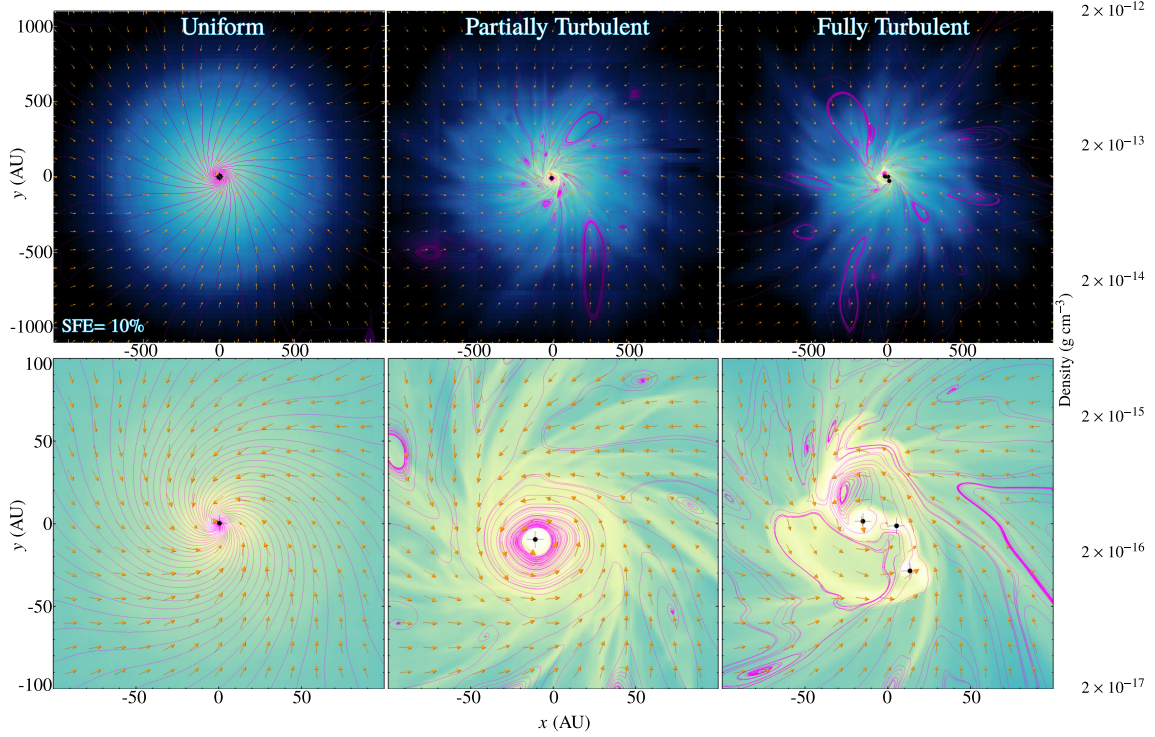| Model	Outflow mass efficiency	Outflow momentum efficiency	Sink formation time	Outflow launching time
Uniform	1.00	1.00	35 120 yr	35 260 yr
Partially turbulent	1.00	0.71	35 353 yr	35 273 yr
Fully turbulent	2.15×10^{-4}	4.45×10^{-5}	34 943 yr	–

Figure 5. Similar to Fig. 3 but in the *xy*-plane. The characteristic time of SFE = 10 per cent is shown for each simulation. In both of these panels, the slice in the *xy*-plane (with thickness of $\Delta z = 100$ au in all cases) is centred on the *z* position of the sink particle (or on the average *z* position of the three sink particles in the fully turbulent case). The slice is centred around (0,0) in the *x* and *y* directions. The colour bar shows average gas density in the slice. Top: As in Fig. 3, the dimensions of these panels are (2200,2200,100) au. Bottom: A zoomed-in view of the top panel, with dimensions (200,200,100) au. It should be noted that the structure of the magenta streamlines representing the magnetic field lines depends on the integration, domain, sampling rate and step size chosen. We have chosen these conditions in such a way as to best represent the underlying physical structure of the field.
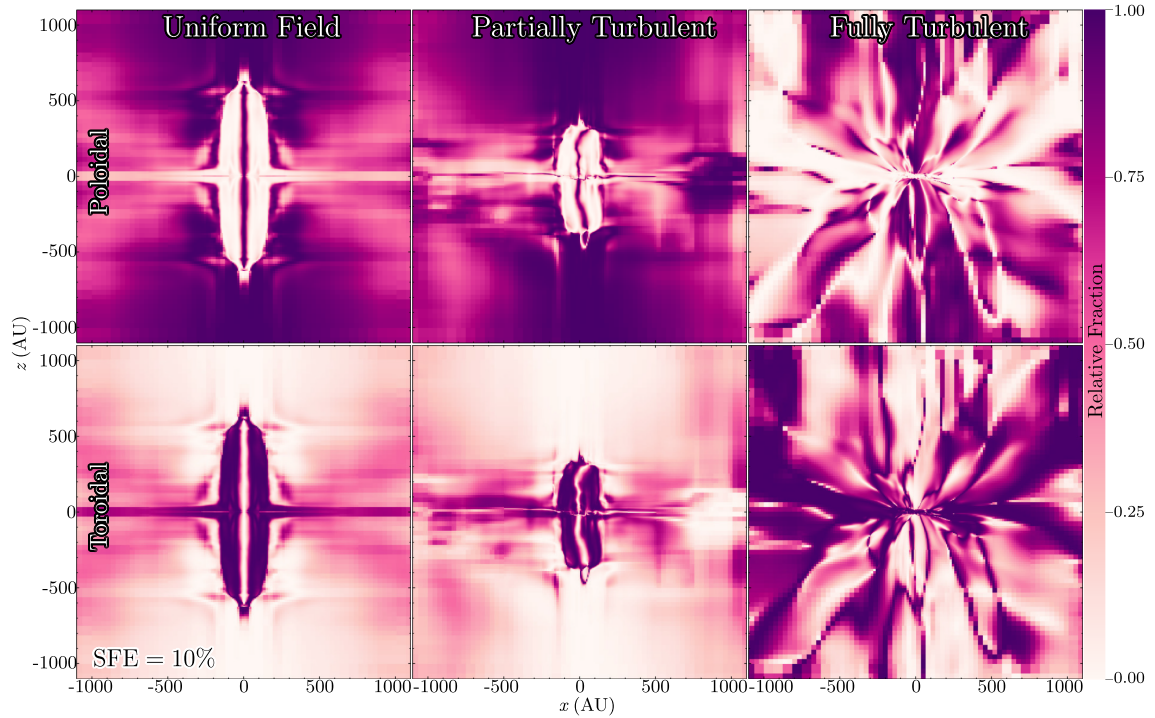
Figure 6. The poloidal and toroidal field components as a relative fraction of total field strength, shown in the *xz*-plane. These values are the average field strength in a slice of the same size as in Fig. 3. Top: The poloidal field fraction for each case, $B_z^2/(B_x^2 + B_y^2 + B_z^2)$. Bottom: The toroidal field fraction for each case, $(B_x^2 + B_y^2)/(B_x^2 + B_y^2 + B_z^2)$.

scale resolved in our simulations is 3 au, which is larger than the scales on which Ohmic diffusivity is important (Shu et al. 2006; Königl & Salmeron 2011). The Hall effect dominates on scales of $1-10$ au (Königl & Salmeron 2011), but its influence on outflow formation is strongly dependant on the angle between the magnetic field and rotation axis of the cloud (e.g. see Wardle & Ng 1999 for an analytic discussion; see numerical examples in Tsukamoto et al. 2015; Wurster et al. 2016; Wurster, Bate & Price 2018c). The random orientation of the initial magnetic field in the fully turbulent case could result in regions of the field being anti-aligned with the rotation axis of the cloud. In such a scenario, the inclusion of Hall effect may cause the outflow of material to be suppressed (e.g. Wurster et al. 2018c), but we do not expect that this effect would increase the likelihood of outflows developing in the fully turbulent case.

The effects of Ohmic resistivity and ambipolar diffusion are independent of the orientation of the magnetic field. For this reason, we expect that our results would be uniformly impacted by the inclusion of these effects, regardless of the initial field morphology. Simulations by Wurster et al. (2016) show that the inclusion of Ohmic resistivity has little impact on the formation jets or their structure. It should be noted that ambipolar diffusion, which dominates on larger scales where the density is low and the fractional ionization is high (Braiding & Wardle 2012), may suppress outflows and effect their morphology, although they are still expected to form at later times (Vaytet et al. 2018). Non-ideal MHD calculations are computationally intensive (Nolan et al. 2017; Wurster et al. 2018b), so we leave it to follow-up studies to include non-ideal MHD and discuss the results in the context of this work. However, the fact that all our simulations use the same ideal MHD approximation still gives a qualitative sense of the relative importance of the magnetic field structure on disc morphology and jet/outflow properties.

4.3.2 The effects of radiation

Radiation is an important aspect of star formation. Radiative feedback has been found to hinder disc fragmentation in some cases (Offner et al. 2009; Price & Bate 2009; Kuiper, Turner & Yorke 2016; Federrath, Krumholz & Hopkins 2017; Guszejnov et al. 2018), while radiation transport plays a role in shaping the temperature and density structure of the protostellar disc. The inclusion of radiative effects in our study may have changed the absolute structure of the discs in each of our models. It is not, however, expected to emphasise the importance of the magnetic field structure in any of our models (relative to each other), when compared to simulations without radiative effects.

4.3.3 Numerical resolution

The highest level of refinement used in our simulations is $L_{ref} = 11$ which corresponds to a cell length of 3.05 au on the highest level of AMR. The minimum refinement is $L_{ref} = 4$, the length of these cells being 125 au. We chose this level of refinement based on convergence tests carried out by Kuruwita et al. (2017), given that our initial set-up closely resembles that work. Federrath et al. (2014) find that full convergence in a domain of this size would require $L_{ref} = 17$. This would result in sub-au resolution ($\Delta x = 0.6$ au), and enable us to better resolve the launching velocities of the jets/outflows. Although the absolute outflow mass and momentum are not converged at $L_{ref} = 11$, the outflow quantities in the partially turbulent and fully turbulent cases as a fraction of the uniform case

are none the less representative of the same relative fractions that would be computed at higher resolutions. Future studies should aim to investigate the results of this work in simulations with higher levels of refinement. Increasing the resolution would also benefit the investigation of non-ideal effects, as discuss in Section 4.3.1.

5 CONCLUSIONS

We have conducted a systematic numerical study of the effects of uniform and turbulent magnetic fields on the formation of bipolar jets and outflows from protostellar discs, and analysed their morphology and efficiency. The behaviour of each of the three cases is as follows:

(i) The uniform case produces a highly collimated jet and forms a single protostar. The jet is launched via a magneto-centrifugal mechanism at a similar time to protostar formation. 500 yr after SFE = 1 per cent the outflowing material has characteristic velocities of $3.16\,\mathrm{km\,s^{-1}}$. The jet in this model is the most effective at transporting mass and momentum away from the disc, causing the initial accretion phase to be less efficient than in the partially turbulent case.

(ii) The partially turbulent case produced definite outflows with a weakly collimated, asymmetric morphology. The outflow was launched before SFE reached 1 per cent, likely due to strong initial accretion. 500 yr after SFE = 1 per cent the outflowing material has characteristic velocities of $1.78\,\mathrm{km\,s^{-1}}$. The launching mechanism in this case is likely a combination of weak magneto-centrifugal forces and magnetic pressure gradient. The wide angle outflows in this model were comparable to that of the uniform case in mass, and 29 per cent less efficient in momentum. This model formed a single protostar.

(iii) The fully turbulent case produced no definite bipolar outflows, and the fractional transport efficiency in comparison to the uniform case is negligible (0.021 per cent in mass and 0.0045 per cent in momentum). 500 yr after SFE = 1 per cent the outflowing material has characteristic velocities of $0.32\,\mathrm{km\,s^{-1}}$. The turbulent magnetic field induced fragmentation of the disc in this model, forming five protostars in total. Accretion was initially inhibited by the isotropy of magnetic pressure.

This study explored the extrema of the effects of magnetic field structure on jet and outflow formation (fully ordered to fully turbulent). The partially turbulent case is the most physically realistic, and future work should be done to examine the parameter space around this midpoint, including a partially turbulent field with a misaligned uniform, poloidal component of the kind discussed in Section 1.

REFERENCES

Bally J., Reipurth B., 2001, ApJ, 546, 299

Banerjee R., Pudritz R. E., 2006, ApJ, 641, 949

Bate M. R., 2015, in Rucinski S. M., Torres G., Zejda M., eds, ASP Conf. Ser. Vol. 496. Living Together: Planets, Host Stars and Binaries. Astron. Soc. Pac., San Francisco, p. 37

Bate M. R., Tricco T. S., Price D. J., 2014, MNRAS, 437, 77

Blandford R. D., Payne D. G., 1982, MNRAS, 199, 883

Braiding C. R., Wardle M., 2012, MNRAS, 422, 261

Brandenburg A., Subramanian K., 2005, Phys. Rep., 417, 1

Chapman N. L. et al., 2013, ApJ, 770, 151

Childs H. et al., 2012, High Performance Visualization–Enabling Extreme-Scale Scientific Insight. Univ. California, California, p. 357

Ching T.-C., Lai S.-P., Zhang Q., Girart J. M., Qiu K., Liu H. B., 2017, ApJ, 838, 121

Ciardi A., Hennebelle P., 2010, MNRAS, 409, L39

Cox E. G., Harris R. J., Looney L. W., Li Z.-Y., Yang H., Tobin J. J., Stephens I., 2018, ApJ, 855, 92

Crutcher R. M., 1999, ApJ, 520, 706

Crutcher R. M., 2012, ARA&A, 50, 29

Dedner A., Kemm F., Kröner D., Munz C.-D., Schnitzer T., Wesenberg M., 2002, J. Comput. Phys., 175, 645

Dubey A. et al., 2008, in Pogorelov N. V., Audit E., Zank G. P., eds, ASP Conf. Ser. Vol. 385, Numerical Modeling of Space Plasma Flows. Astron. Soc. Pac., San Francisco, p. 145

Dubinski J., Narayan R., Phillips T. G., 1995, ApJ, 448, 226

Duchêne G., Kraus A., 2013, ARA&A, 51, 269

Elmegreen B. G., Scalo J., 2004, ARA&A, 42, 211

Evans C. R., Hawley J. F., 1988, ApJ, 332, 659

Federrath C., 2015, MNRAS, 450, 4035

Federrath C., 2016, J. Plasma Phys., 82, 535820601

Federrath C., Klessen R. S., 2012, ApJ, 761, 156

Federrath C., Roman-Duval J., Klessen R. S., Schmidt W., Mac Low M.-M., 2010a, A&A, 512, A81

Federrath C., Banerjee R., Clark P. C., Klessen R. S., 2010b, ApJ, 713, 269

Federrath C., Chabrier G., Schober J., Banerjee R., Klessen R. S., Schleicher D. R. G., 2011a, Phys. Rev. Letters, 107, 114504

Federrath C., Sur S., Schleicher D. R. G., Banerjee R., Klessen R. S., 2011b, ApJ, 731, 62

Federrath C., Schrön M., Banerjee R., Klessen R. S., 2014, ApJ, 790, 128

Federrath C., Krumholz M., Hopkins P. F., 2017, J. Phys. Conf. Ser., 837, p. 012007

Frank A. et al., 2014, in Beuther H., Klessen R. S., Dullemond C. P., Henning T., eds, Protostars and Planets VI. Univ. Arizona Press, Tucson, p. 451

Fryxell B. et al., 2000, ApJS, 131, 273

Gardiner T. A., Stone J. M., 2005, J. Comput. Phys., 205, 509

Girart J. M., Frau P., Zhang Q., Koch P. M., Qiu K., Tang Y.-W., Lai S.-P., Ho P. T. P., 2013, ApJ, 772, 69

Glover S. C. O., Clark P. C., 2012, MNRAS, 426, 377

Glover S. C. O., Mac Low M.-M., 2007a, ApJS, 169, 239

Glover S. C. O., Mac Low M.-M., 2007b, ApJ, 659, 1317

Glover S. C. O., Federrath C., Mac Low M.-M., Klessen R. S., 2010, MNRAS, 404, 2

Gray W. J., McKee C. F., Klein R. I., 2018, MNRAS, 473, 2124

Guszejnov D., Hopkins P. F., Grudic M. Y., Krumholz M. R., Federrath C., 2018, MNRAS, 480, 182

Hennebelle P., Ciardi A., 2009, A&A, 506, L29

Hennebelle P., Falgarone E., 2012, A&AR, 20, 55

Hennebelle P., Fromang S., 2008, A&A, 477, 9

Hennemann M. et al., 2012, A&A, 543, L3

Heyer M. H., Brunt C. M., 2004, ApJ, 615, L45

Hill T. et al., 2011, A&A, 533, A94

Hull C. L. H. et al., 2017, ApJ, 847, 92

Joos M., Hennebelle P., Ciardi A., 2012, A&A, 543, A128

Joos M., Hennebelle P., Ciardi A., Fromang S., 2013, A&A, 554, A17

Kazantsev A. P., 1968, Sov. J. Exp. Theor. Phys., 26, 1031

King P. K., Fissel L. M., Chen C.-Y., Li Z.-Y., 2018, MNRAS, 474, 5122

Königl A., Salmeron R., 2011, The Effects of Large-Scale Magnetic Fields on Disk Formation and Evolution. Univ. Chicago Press, Chicago, IL, p. 283

Krumholz M. R., 2014, Phys. Rep., 539, 49

Krumholz M. R., Crutcher R. M., Hull C. L. H., 2013, ApJ, 767, L11

Kuiper R., Turner N. J., Yorke H. W., 2016, ApJ, 832, 40

Kuruwita R. L., Federrath C., Ireland M., 2017, MNRAS, 470, 1626

Larson R. B., 1981, MNRAS, 194, 809

Lazarian A., Hoang T., 2007, MNRAS, 378, 910

Lewis B. T., Bate M. R., 2017, MNRAS, 467, 3324

Lewis B. T., Bate M. R., 2018, MNRAS, 477, 4241

Lewis B. T., Bate M. R., Price D. J., 2015, MNRAS, 451, 288

Li Z.-Y., Krasnopolsky R., Shang H., 2013, ApJ, 774, 82

Li H.-B., Goodman A., Sridharan T. K., Houde M., Li Z.-Y., Novak G., Tang K. S., 2014, in Beuther H., Klessen R. S., Dullemond C. P., Henning T., eds, Protostars and Planets VI. Univ. Arizona Press, Tucson, p. 101

Li Z.-Y., Krasnopolsky R., Shang H., Zhao B., 2014, ApJ, 793, 130

Lynden-Bell D., 2003, MNRAS, 341, 1360

Mac Low M.-M., Klessen R. S., 2004, Rev. Mod. Phys., 76, 125

Machida M. N., Omukai K., Matsumoto T., Inutsuka S.-i., 2006, ApJ, 647, L1

Machida M. N., Inutsuka S.-i., Matsumoto T., 2008, ApJ, 676, 1088

Marder B., 1987, J. Comput. Phys., 68, 48

Masunaga H., Inutsuka S.-i., 2000, ApJ, 531, 350

McKee C. F., Ostriker E. C., 2007, ARA&A, 45, 565

Mouschovias T. C., Spitzer L., Jr., 1976, ApJ, 210, 326

Nolan C. A., Salmeron R., Federrath C., Bicknell G. V., Sutherland R. S., 2017, MNRAS, 471, 1488

Offner S. S. R., Klein R. I., McKee C. F., Krumholz M. R., 2009, ApJ, 703, 131

Omukai K., Tsuribe T., Schneider R., Ferrara A., 2005, ApJ, 626, 627

Ossenkopf V., Mac Low M.-M., 2002, A&A, 390, 307

Padoan P. et al., 2014, in Beuther H., Klessen R. S., Dullemond C. P., Henning T., eds, Protostars and Planets VI. Univ. Arizona Press, Tucson, p. 77

Pattle K. et al., 2017, ApJ, 846, 122

Pavlovski G., Smith M. D., Mac Low M.-M., 2006, MNRAS, 368, 943

Planck Collaboration XXXIII, 2016, A&A, 586, A136

Price D. J., Bate M. R., 2007, MNRAS, 377, 77

Price D. J., Bate M. R., 2009, MNRAS, 398, 33

Price D. J., Tricco T. S., Bate M. R., 2012, MNRAS, 423, L45

Pudritz R. E., Norman C. A., 1986, ApJ, 301, 571

Pudritz R. E., Ouyed R., Fendt C., Brandenburg A., 2007, in Reipurth B., Jewitt D., Keil K., eds, Protostars and Planets V. Univ. Arizona Press, Tucson, p. 277

Roman-Duval J., Federrath C., Brunt C., Heyer M., Jackson J., Klessen R. S., 2011, ApJ, 740, 120

Schleicher D. R. G., Schober J., Federrath C., Bovino S., Schmidt W., 2013, New J. Phys., 15, 023017

Schober J., Schleicher D., Bovino S., Klessen R. S., 2012a, Phys. Rev. E, 86, 066412

Schober J., Schleicher D., Federrath C., Glover S., Klessen R. S., Banerjee R., 2012b, ApJ, 754, 99

Shang H., Allen A., Li Z.-Y., Liu C.-F., Chou M.-Y., Anderson J., 2006, ApJ, 649, 845

Shu F. H., Galli D., Lizano S., Cai M., 2006, ApJ, 647, 382

Stojimirović I., Narayanan G., Snell R. L., Bally J., 2006, ApJ, 649, 280

Sur S., Schleicher D. R. G., Banerjee R., Federrath C., Klessen R. S., 2010, ApJ, 721, L134

Tomida K., Tomisaka K., Matsumoto T., Ohsuga K., Machida M. N., Saigo K., 2010, ApJ, 714, L58

Tricco T. S., Price D. J., Bate M. R., 2016, J. Comput. Phys., 322, 326

Truelove J. K., Klein R. I., McKee C. F., Holliman J. H., II, Howell L. H., Greenough J. A., 1997, ApJ, 489, L179

Tsukamoto Y., Iwasaki K., Okuzumi S., Machida M. N., Inutsuka S., 2015, ApJ, 810, L26

Turk M. J., Smith B. D., Oishi J. S., Skory S., Skillman S. W., Abel T., Norman M. L., 2011, ApJS, 192, 9

Vaytet N., Commerçon B., Masson J., González M., Chabrier G., 2018, A&A, 615, A5

Waagan K., Federrath C., Klingenberg C., 2011, J. Comput. Phys., 230, 3331

Wardle M., Ng C., 1999, MNRAS, 303, 239

Wolfire M. G., Hollenbach D., McKee C. F., Tielens A. G. G. M., Bakes E. L. O., 1995, ApJ, 443, 152

Wu Y., Wei Y., Zhao M., Shi Y., Yu W., Qin S., Huang M., 2004, A&A, 426, 503

Wünsch R., Walch S., Dinnbier F., Whitworth A., 2018, MNRAS, 475, 3393

Wurster J., Price D. J., Bate M. R., 2016, MNRAS, 457, 1037

Wurster J., Bate M. R., Price D. J., 2018a, MNRAS, 475, 1859

Wurster J., Bate M. R., Price D. J., 2018b, MNRAS, 476, 2063

Wurster J., Bate M. R., Price D. J., 2018c, MNRAS, 480, 4434

This paper has been typeset from a TEX/LATEX file prepared by the author.